



HAL
open science

Solar wind current sheets and deHoffmann-Teller analysis. First results from Solar Orbiter's DC electric field measurements

K. Steinvall, Yu. V. Khotyaintsev, G. Cozzani, A. Vaivads, E. Yordanova, A. I. Eriksson, N. J. T. Edberg, M. Maksimovic, S. D. Bale, Thomas Chust, et al.

► To cite this version:

K. Steinvall, Yu. V. Khotyaintsev, G. Cozzani, A. Vaivads, E. Yordanova, et al.. Solar wind current sheets and deHoffmann-Teller analysis. First results from Solar Orbiter's DC electric field measurements. *Astronomy & Astrophysics - A&A*, 2021, 656, 7 pp. <10.1051/0004-6361/202140855>. <hal-03536592>

HAL Id: hal-03536592

<https://hal.science/hal-03536592v1>

Submitted on 17 Jun 2022

HAL is a multi-disciplinary open access archive for the deposit and dissemination of scientific research documents, whether they are published or not. The documents may come from teaching and research institutions in France or abroad, or from public or private research centers.

L'archive ouverte pluridisciplinaire HAL, est destinée au dépôt et à la diffusion de documents scientifiques de niveau recherche, publiés ou non, émanant des établissements d'enseignement et de recherche français ou étrangers, des laboratoires publics ou privés.



HAL Authorization

Solar wind current sheets and deHoffmann-Teller analysis

First results from Solar Orbiter's DC electric field measurements

K. Steinvall^{1,2}, Yu. V. Khotyaintsev¹, G. Cozzani¹, A. Vaivads³, E. Yordanova¹, A. I. Eriksson¹, N. J. T. Edberg¹, M. Maksimovic⁴, S. D. Bale^{5,6}, T. Chust⁷, V. Krasnoselskikh^{8,5}, M. Kretzschmar^{8,9}, E. Lorfèvre¹⁰, D. Plettemeier¹¹, J. Souček¹², M. Steller¹³, Š. Štverák¹⁴, A. Vecchio^{4,15}, T. S. Horbury¹⁶, H. O'Brien¹⁶, V. Evans¹⁶, A. Fedorov¹⁷, P. Louarn¹⁷, V. Génot¹⁷, N. André¹⁷, B. Lavraud^{17,18}, A. P. Rouillard¹⁷, and C. J. Owen¹⁹

(Affiliations can be found after the references)

Received 22 March 2021 / Accepted 26 April 2021

ABSTRACT

Context. Solar Orbiter was launched on 10 February 2020 with the purpose of investigating solar and heliospheric physics using a payload of instruments designed for both remote and in situ studies. Similar to the recently launched Parker Solar Probe, and unlike earlier missions, Solar Orbiter carries instruments designed to measure low-frequency DC electric fields.

Aims. In this paper, we assess the quality of the low-frequency DC electric field measured by the Radio and Plasma Waves instrument (RPW) on Solar Orbiter. In particular, we investigate the possibility of using Solar Orbiter's DC electric and magnetic field data to estimate the solar wind speed.

Methods. We used a deHoffmann-Teller (HT) analysis, based on measurements of the electric and magnetic fields, to find the velocity of solar wind current sheets, which minimises a single component of the electric field. By comparing the HT velocity to the proton velocity measured by the Proton and Alpha particle Sensor (PAS), we have developed a simple model for the effective antenna length, L_{eff} of the E-field probes. We then used the HT method to estimate the speed of the solar wind.

Results. Using the HT method, we find that the observed variations in E_y are often in excellent agreement with the variations in the magnetic field. The magnitude of E_y , however, is uncertain due to the fact that the L_{eff} depends on the plasma environment. Here, we derive an empirical model relating L_{eff} to the Debye length, which we can use to improve the estimate of E_y and, consequently, the estimated solar wind speed.

Conclusions. The low-frequency electric field provided by RPW is of high quality. Using the deHoffmann-Teller analysis, Solar Orbiter's magnetic and electric field measurements can be used to estimate the solar wind speed when plasma data are unavailable.

Key words. solar wind – plasmas – magnetic reconnection – methods: data analysis

1. Introduction

With the recent launch of NASA's Parker Solar Probe (Fox & McComas 2016) and ESA's Solar Orbiter (Müller et al. 2020), the low-frequency 'DC' electric field, \mathbf{E} , associated with the solar wind, can be measured for the first time at heliocentric distances below 1 AU. The electric field is one of the most challenging quantities to measure. One significant complication is that the spacecraft and its solar panels are charged to some variable potential and will generate an electrostatic field, which is not of physical interest (Cully et al. 2007; Johansson et al. 2020). Another difficulty is that the E-field probes must be adequately separated to provide the sensitivity necessary to measure weak electric fields in plasma. To investigate the quality of the E-field measurement, it can often be useful to analyse large-scale fluctuations in the magnetic field, \mathbf{B} . Since the solar wind plasma is, on large scales, in the ideal MHD state, \mathbf{E} is related to \mathbf{B} via the simple formula $\mathbf{E} = -\mathbf{v} \times \mathbf{B}$, where \mathbf{v} is the plasma bulk velocity. Thus, if a magnetic structure, such as a current sheet, crosses the spacecraft at a constant \mathbf{v} , then the \mathbf{E} fluctuations linearly related to the fluctuations in \mathbf{B} will be observed. Moreover, if the plasma velocity is measured independently, it is possible to calculate the electric field as $\mathbf{E} = -\mathbf{v} \times \mathbf{B}$ and compare the results directly to the measured E-field as a method of quality control (Mozer et al. 2020a).

When analysing magnetic structures such as current sheets, Alfvén waves, or shocks, it is often necessary to find

the proper frame of the structure. This is commonly done using deHoffmann-Teller analysis (De Hoffmann & Teller 1950; Sonnerup et al. 1987). The proper frame of a magnetic structure is a deHoffmann-Teller (HT) frame if $\mathbf{E} = 0$ in it. Thus, if the HT frame exists, the electric field in the spacecraft frame is given by $\mathbf{E} = -\mathbf{v}_{\text{HT}} \times \mathbf{B}$, where the HT velocity \mathbf{v}_{HT} is the velocity of the HT frame with respect to the spacecraft frame. We note that we cannot transform away any component of \mathbf{E} parallel to \mathbf{B} (E_{\parallel}). However, on the large scales we are interested in, E_{\parallel} is typically zero. Historically, HT analysis has been used extensively to analyse shocks (e.g., Schwartz et al. 1988; Lefebvre et al. 2007) and magnetic reconnection at Earth's magnetopause (e.g., Fuselier et al. 1991; Phan et al. 2004) and in the solar wind (e.g., Gosling et al. 2005). More recently, Horbury et al. (2020a) used HT analysis to find the proper frame of large-scale solar wind spikes (Horbury et al. 2018), also known as 'switchbacks' (e.g., Bale et al. 2019; Mozer et al. 2020b), observed by Parker Solar Probe. Also, Němeček et al. (2020a) applied a HT analysis to particle velocity data in the solar wind, concluding that the HT frame can be considered a proper solar wind frame.

Another important application of the HT analysis, which to the best of our knowledge has not been previously reported, is to estimate the solar wind speed in the absence of particle data. Fluctuations in the solar wind magnetic field are primarily either frozen-in current sheets or MHD turbulence (Borovsky 2010). The HT frame of a current sheet is the frame in which $\mathbf{E} = 0$

on both sides of the discontinuity. In other words, it is the frame in which the plasma flow is field aligned on both sides. In the solar wind, the plasma flow is usually approximately constant across the discontinuity, while \mathbf{B} is arbitrarily rotated in the plane of the discontinuity, implying \mathbf{v} cannot be field-aligned simultaneously on both sides (unless the fields are exactly parallel or anti-parallel, in which case \mathbf{v}_{HT} is not unique, as discussed by Khrabrov & Sonnerup 1998). It thus follows that if a HT frame exists, \mathbf{v} must be zero in it, implying $\mathbf{v}_{\text{HT}} = \mathbf{v}$. Therefore, by applying the HT analysis to solar wind current sheets, which are often tangential discontinuities (Knetter et al. 2004), we obtain a measure of the solar wind velocity. For completeness we note that while rotational discontinuities always have a HT frame, there is a specific theoretical configuration in which tangential discontinuities do not have a HT frame. In this special configuration, the magnetic fields on the two sides of the discontinuity are perfectly parallel or anti-parallel, while the plasma flow has a different perpendicular (to \mathbf{B}) component on the two sides of the discontinuity (Khrabrov & Sonnerup 1998). However, due to the strict criteria on the magnetic fields, this situation does not occur in practice, and the discontinuities we observe in the solar wind should always have a HT frame.

If we instead apply the HT analysis on an Alfvénic structure, Faraday’s law implies that \mathbf{v}_{HT} is the phase velocity of the structure. In the spacecraft frame, this gives $\mathbf{v}_{\text{HT}} = \mathbf{v} + \mathbf{v}_\phi$, where \mathbf{v}_ϕ is the phase velocity in the plasma frame, which depends on the wave-mode and propagation direction, and typically is on the order of the Alfvén speed v_A . Far from the Sun, v_A is small compared to \mathbf{v} , and we can treat it as a small correction to the solar wind speed. However, closer to the Sun, this extra contribution might become non-negligible when analysing Alfvénic structures such as switchbacks, as discussed by Horbury et al. (2020a).

To avoid potential confusion, we want to emphasise that while the HT velocity is derived from $\mathbf{E} = -\mathbf{v} \times \mathbf{B}$, \mathbf{v}_{HT} is not necessarily perpendicular to the ambient magnetic field. One way to understand this is to realise that we are applying the analysis to magnetic structures which have associated magnetic fluctuations, $\delta\mathbf{B}$, such that $\mathbf{B} = \mathbf{B}_0 + \delta\mathbf{B}$, where \mathbf{B}_0 is the background magnetic field. For simplicity, if \mathbf{v} is constant, the corresponding electric fluctuation is given by

$$\delta\mathbf{E} = -\mathbf{v} \times \delta\mathbf{B}. \quad (1)$$

So even if \mathbf{B}_0 and \mathbf{v} are parallel, as long as $\delta\mathbf{B}$ has a component perpendicular to \mathbf{B}_0 , it can be used together with $\delta\mathbf{E}$ to estimate \mathbf{v} .

In this study, we apply a HT analysis based on electric and magnetic field measurements to solar wind current sheets to investigate the quality of Solar Orbiter’s DC electric field. Once we establish that the quality is sufficient, we apply the HT analysis to estimate the solar wind speed. We find that our method can be used to distinguish between fast and slow solar wind, providing a measure of the solar wind velocity even when particle data are unavailable.

2. Instrumentation and DC E calibration

The data used in this study come from the Solar Orbiter mission. We use magnetic field data from the magnetometer (MAG; Horbury et al. 2020b) sampled at 8 vectors per second, plasma measurements from the Solar Wind Analyser suite (SWA; Owen et al. 2020), in particular, from the Proton and Alpha particle Sensor (PAS) at 0.25 samples per second, and

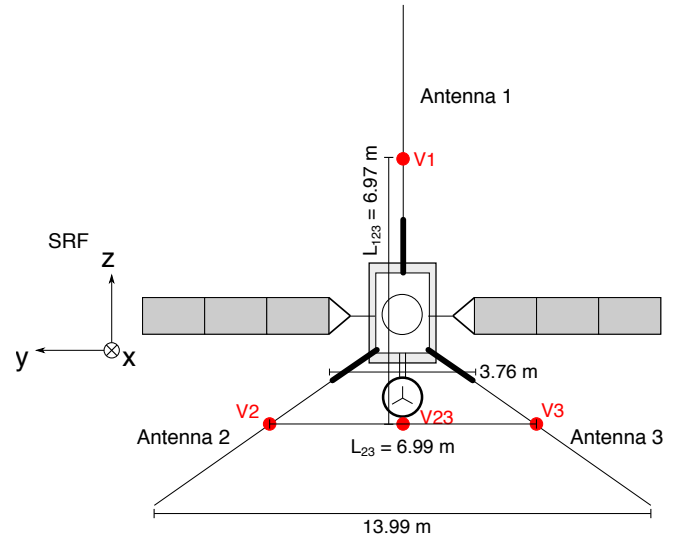


Fig. 1. Qualitative sketch of Solar Orbiter as seen from behind, showing the RPW antennas (i.e. the probes) and the nominal effective antenna lengths L_{23} and L_{123} .

electric fields from the Radio and Plasma Waves instrument (RPW; Maksimovic et al. 2020) sampled at 16 vectors per second. Throughout this paper, we primarily present vector quantities in the spacecraft coordinate system (SRF) defined in such a way that $\hat{\mathbf{x}}$ is pointing away from Solar Orbiter toward the Sun, $\hat{\mathbf{z}}$ is along RPW antenna 1 (approximately normal to the ecliptic plane for the data used in this study, see Fig. 1), and $\hat{\mathbf{y}}$ completes the right-handed coordinate system.

Since the main focus of this study is on the DC electric field \mathbf{E} , we briefly summarise the method used to calculate and calibrate \mathbf{E} , while referring to Maksimovic et al. (2020) for more details about the RPW instrument. The electric field is measured using three cylindrical probes lying in the YZ plane as shown in Fig. 1. RPW measures the probe-to-spacecraft potential for the three probes, V_1 , V_2 , and V_3 , respectively. Since probes 2 and 3 are symmetrically positioned along y with respect to both spacecraft and solar panels, spacecraft effects are mostly cancelled out when computing $E_y = (V_3 - V_2)/L_{23}$, where L_{23} is the nominal effective antenna length (6.99 m), that is, the spatial distance between the measurements of V_2 and V_3 . This, however, is not the case when we compute $E_z = (V_{23} - V_1)/L_{123}$, where $V_{23} = (V_2 + V_3)/2$ is the mean potential of probes 2 and 3, and L_{123} is the nominal effective antenna length (6.97 m) in the z -direction, since probe 1 is placed in a different potential environment compared to probes 2 and 3. As a result, E_z does not behave as well as E_y , and tends to be more noisy. Consequently, throughout this investigation, we only use E_y , which is sufficient for the purposes of this study.

In the ideal case E_y can be directly computed as $E_y = (V_3 - V_2)/L_{23}$. In reality however, the probe signals may have instrumental offsets which we need to compensate for. The source of the offsets can for example be a difference in characteristics of the individual probes, asymmetries in the electrostatic potential of the spacecraft and solar panels, and plasma wakes. We account for these by taking a large window (several hours) of data and fitting V_2 against V_3 linearly to find a slope k_{23} , and offset d_{23} . Typically, k_{23} is steady and very close to 1, and we set it to be identically 1 throughout this study. The offset is more variable with a typical value of $\sim d_{23} = 0.1$ V. We therefore correct V_2 for the offset $V_2' = V_2 - d_{23}$. This

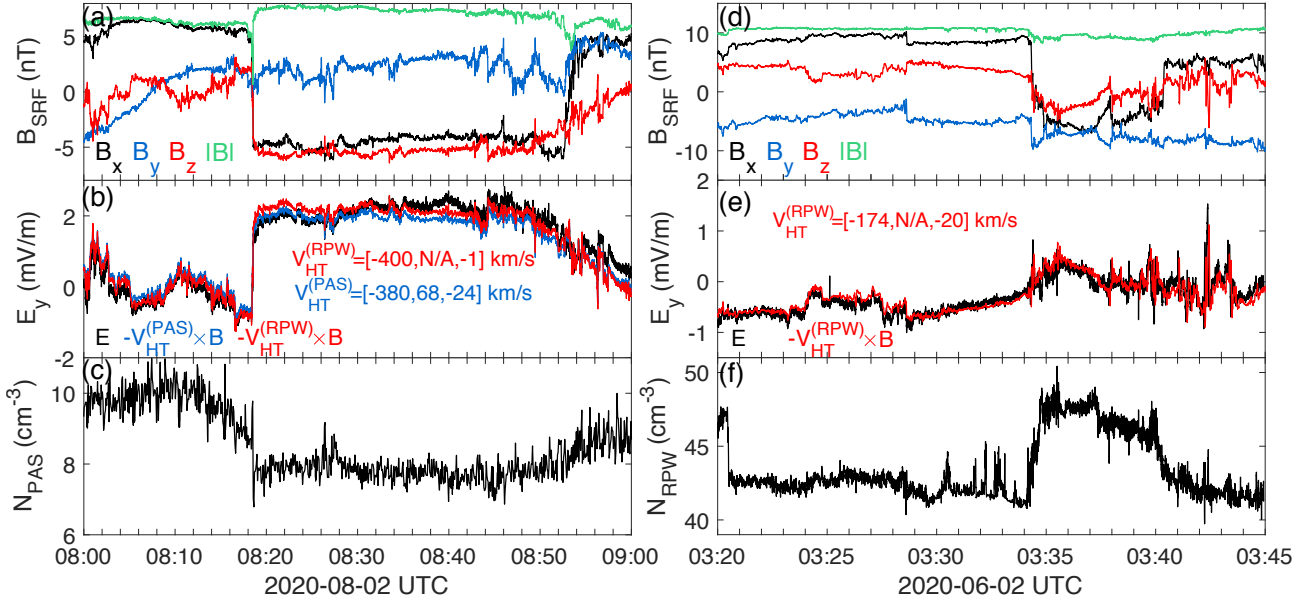


Fig. 2. Current sheet crossings at different heliocentric distances (left column 0.75 AU, right column 0.54 AU). *Panel a:* magnetic field in SRF coordinates. *Panel b:* E_y (black) and $-(\mathbf{v}_{\text{HT}} \times \mathbf{B})_y$ with \mathbf{v}_{HT} from PAS (blue) and RPW (red). *Panel c:* plasma density from PAS. *Panels d–f:* same format as *a–c* for a different current sheet where PAS data are unavailable. Plasma density was estimated from the spacecraft potential (Khotyaintsev et al. 2021).

correction implicitly assumes that $E_y = 0$ on the time-scale of the window. One additional complication we occasionally need to account for is that we sometimes find an unphysical correlation between $V'_2 - V_3$ and $V'_2 + V_3$, that is, a correlation between E_y and the spacecraft potential. When this correlation is strong and the absolute value of the correlation coefficient between the two terms exceeds 0.7, we add an additional step to the calibration to remove this common mode signal. This step is to fit $V'_2 - V_3$ linearly against $V'_2 + V_3$ yielding an offset Γ_0 and a slope Γ_1 , which we adjust for symmetrically as $V_2^* = V'_2 - [\Gamma_0 + \Gamma_1(V'_2 + V_3)]/2$, $V_3^* = V_3 + [\Gamma_0 + \Gamma_1(V'_2 + V_3)]/2$. We can then finally compute E_y as $E_y = (V_3^* - V_2^*)/L_{23}$.

3. Current sheets and the deHoffmann-Teller analysis

To validate E_y , we make use of fact that the plasma is in the ideal MHD state, meaning $\mathbf{E} = -\mathbf{v} \times \mathbf{B}$. Since the solar wind velocity is relatively steady if compared to the magnetic field, which changes significantly in both magnitude and direction, variations in \mathbf{E} correspond primarily to variations in \mathbf{B} . Because of this, current sheet crossings serve as an excellent opportunity to test the DC \mathbf{E} measurements using the HT analysis. In this study, we calculate \mathbf{v}_{HT} in two ways. Firstly, following the theory discussed by Khrabrov & Sonnerup (1998) and Paschmann & Sonnerup (2008), dropping the contribution of E_x, E_z, B_y and v_y results in

$$\begin{pmatrix} \langle E_y B_z \rangle \\ -\langle E_y B_x \rangle \end{pmatrix} = \begin{pmatrix} \langle B_z^2 \rangle & -\langle B_x B_z \rangle \\ -\langle B_x B_z \rangle & \langle B_x^2 \rangle \end{pmatrix} \begin{pmatrix} v_{\text{HT},x} \\ v_{\text{HT},z} \end{pmatrix}, \quad (2)$$

where $\langle \cdot \rangle$ denotes averaging. Solving for \mathbf{v}_{HT} , we find the velocity of the frame in which $E_y = 0$. What is evident from Eq. (2) is the fact that we are unable to determine $v_{\text{HT},y}$, and \mathbf{v}_{HT} is not unique in that respect. However, the solar wind is mainly expanding radially from the Sun, so that $|v_x| \gg |v_y|$ (Němeček et al. 2020b), and the observed v_y is mainly due to orbital motion of the spacecraft, which is rarely of practical importance. Secondly, when PAS data

are available, we use the 3D ion velocity vectors and Eq. (9.10) from Khrabrov & Sonnerup (1998) to obtain an estimate of \mathbf{v}_{HT} that does not involve \mathbf{E} , which can be compared to the results of Eq. (2).

In Fig. 2, we present two examples of current sheets identified as sharp rotations in at least one component of \mathbf{B} , where we apply the HT analysis. For the first current sheet (observed at 0.75 AU), there are PAS data available and we use both methods to calculate \mathbf{v}_{HT} . We show the results in Fig. 2b, where we plot E_y (black) together with $-(\mathbf{v}_{\text{HT}} \times \mathbf{B})_y$, where \mathbf{v}_{HT} was obtained using RPW data with Eq. (2) (red), as well as PAS data using Eq. (9.10) from Khrabrov & Sonnerup (1998) (blue). The two \mathbf{v}_{HT} estimates are in good agreement, $\mathbf{v}_{\text{HT}}^{(\text{RPW})} = [-400, \text{N/A}, -1]$, $\mathbf{v}_{\text{HT}}^{(\text{PAS})} = [-380, 68, -24]$. There is an excellent agreement between E_y and $-\mathbf{v}_{\text{HT}} \times \mathbf{B}$, indicating that the HT frame exists, and that E_y is accurately measured on both large and small scales. The obtained HT velocities are close to the solar wind velocity measured by PAS, $\mathbf{v} = [-370, 64, -18]$ km s⁻¹, which shows that the HT method indeed can be used to estimate the solar wind speed. For reference, the average Alfvén speed in this interval is 35 km s⁻¹. The second current sheet (Figs. 2d–f) was observed closer to the Sun, at 0.54 AU, and there was no particle data from PAS for a comparison. Using the spacecraft potential and plasma frequency measured by RPW we estimate the plasma density (Khotyaintsev et al. 2021) shown in Fig. 2f, and find an average Alfvén speed of 34 km s⁻¹. The results of the HT analysis in Fig. 2e shows a good agreement between E_y and $-(\mathbf{v}_{\text{HT}} \times \mathbf{B})_y$, suggesting again that the HT frame exists and that E_y accurately follows the changes in \mathbf{B} . However, we note the low value of $\mathbf{v}_{\text{HT}}^{(\text{RPW})} = [-174, \text{N/A}, -20]$ km s⁻¹ compared to the typical solar wind velocity, which suggests that the magnitude of E_y is underestimated. This is likely related to the effective antenna length L_{eff} , being shorter than the nominal length $L_{23} = 6.99$ m used in the calibration leading to both E_y and \mathbf{v}_{HT} being underestimated.

The first current sheet (Figs. 2a–c) had a small magnetic field component that was normal to the current sheet

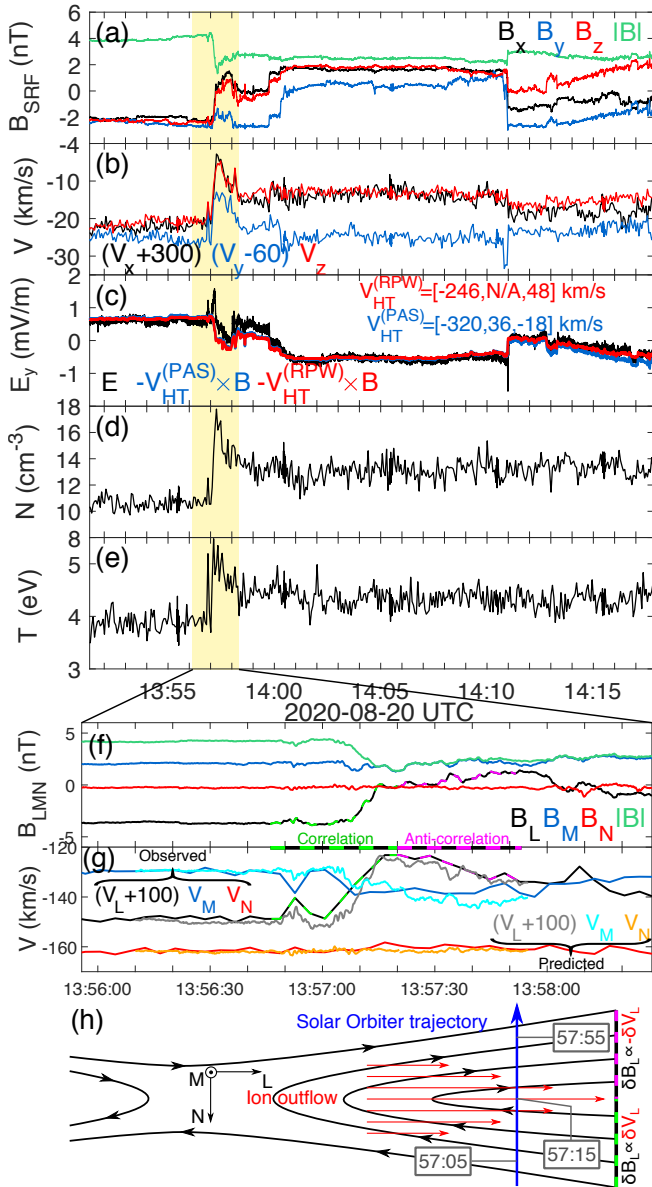


Fig. 3. Observations of a reconnecting current sheet. *Panels a,b:* magnetic field and ion velocity in SRF. *Panel c:* E_y and $-(\mathbf{v}_{\text{HT}} \times \mathbf{B})_y$ with \mathbf{v}_{HT} from PAS (blue) and RPW (red). *Panels d,e:* ion density and temperature from PAS. *Panel f:* magnetic field in LMN coordinates at the reconnection jet. *Panel g:* observed (black, blue, red) and predicted (green, cyan, orange) plasma velocities in LMN coordinates. The green and magenta dashed horizontal bars highlight where B_L and V_L are correlated and anti-correlated, respectively. *Panel h:* simplified sketch of the reconnection event illustrating the expected correlation and anti-correlation between B_L and V_L .

$B_n \approx 0.2$ nT, $B_n/|\mathbf{B}| \approx 0.04$, obtained using minimum variance analysis (Sonnerup & Cahill 1967), and the plasma data showed no signatures of reconnection. The second current sheet (Figs. 2d–f) had a much larger normal component $B_n \approx 1.5$ nT, $B_n/|\mathbf{B}| \approx 0.15$, but no plasma data were available to compare with. Next, we investigate a current sheet with an intermediate normal magnetic field component $B_n \approx -0.3$ nT, $B_n/|\mathbf{B}| \approx 0.09$, where plasma data, which shows several signatures of magnetic reconnection, were available.

On 20 August 2020, Solar Orbiter observed several sharp \mathbf{B} changes during which B_x changed its sign (i.e. radial polarity changes), often concurrently to significant reductions in

magnetic field magnitude, which occasionally reached values as low as 0.1 nT. The Magnetic Connectivity Tool (Rouillard et al. 2020) shows that Solar Orbiter was very close to the heliospheric current sheet (HCS) during this time, suggesting that these observations were likely multiple crossings of the HCS. In Fig. 3, we present an overview of two such crossings that show signatures of ongoing magnetic reconnection. By applying our HT analysis on the whole interval (Fig. 3c), we are again able to find a good agreement between E_y and $-(\mathbf{v}_{\text{HT}} \times \mathbf{B})_y$, and we conclude that a HT frame exists. The difference between $\mathbf{v}_{\text{HT}}^{(\text{RPW})} = [-246, N/A, 48]$ km s $^{-1}$ and $\mathbf{v}_{\text{HT}}^{(\text{PAS})} = [-320, 36, -18]$ km s $^{-1}$, indicates that $|E_y|$ is underestimated by about 20%. We again find that the average Alfvén speed of 22 km s $^{-1}$ is much slower than the solar wind speed, and the effect of Alfvénic fluctuations are negligible. During the first crossing at 13:57 UT (yellow highlight), there is a clear peak in the plasma velocity (Fig. 3b), which is concurrent with an increase in density (Fig. 3d) and ion temperature (Fig. 3e). These are signatures of a reconnection outflow. In order to investigate whether this observation is consistent with ongoing magnetic reconnection, we use a minimum variance analysis to determine the local current sheet coordinate system (Sonnerup & Cahill 1967). We limit the minimum variance analysis to the first small-scale current sheet highlighted in yellow, and find $L = [0.75, 0.17, 0.64]$, $M = [0.31, -0.94, -0.11]$, $N = [0.58, 0.27, -0.76]$, where N is normal to the current sheet, L is in the direction of the reconnecting \mathbf{B} component, and M points out of the reconnection plane. In Figs. 3f,g we show a zoom-in on the jet, and present \mathbf{B} and \mathbf{v} in LMN coordinates. One important feature in the data is the changing correlation between B_L and v_L , highlighted by the green and magenta dashed lines. During the leading part of the crossing, B_L and v_L are correlated (green dashes), while in the trailing part they are anti-correlated (magenta dashes), consistent with the sketch in Fig. 3h. This signature corresponds to the two Alfvén waves propagating away from the reconnection site, parallel and anti-parallel to \mathbf{B} (e.g., Gosling et al. 2005; Lavraud et al. 2009; Phan et al. 2020; Froment et al. 2021), and distinguishes it from Alfvénic structures such as switchbacks, characterised by a single correlation. We show the results from a more quantitative test of the magnetic reconnection hypothesis, a Walén test, in Fig. 3g, where the overplotted grey, cyan, and orange curves are the predicted velocity components when crossing a rotational discontinuity in an isotropic plasma (Hudson 1970):

$$\mathbf{v}_{\text{predicted}} = \mathbf{v}_{\text{ref}} \pm \left(\frac{\mathbf{B}}{\sqrt{\mu_0 \rho}} - \frac{\mathbf{B}_{\text{ref}}}{\sqrt{\mu_0 \rho_{\text{ref}}}} \right), \quad (3)$$

where ρ is the ion mass density, and the subscript ‘ref’ denotes reference values selected on either side of the jet. The + solution is taken for the leading edge, and – is taken for the trailing edge, while the corresponding time for the reference values are 13:56:10 and 13:57:55 UT. The good agreement between the prediction and observation indicates that Solar Orbiter crossed a rotational discontinuity. Performing the same analysis on similar crossings later in the day (e.g., 16:44:00 UT) yields similar results.

In summary, by applying our HT method on Solar Orbiter data from crossings of current sheets, some of which are undergoing magnetic reconnection, we find that the HT frames exist, and E_y well captures changes in \mathbf{B} . However, due to variations in the effective antenna length, the magnitude of E_y , and consequently also $|\mathbf{v}_{\text{HT}}|$, is not always accurate. We address this issue in the following section.

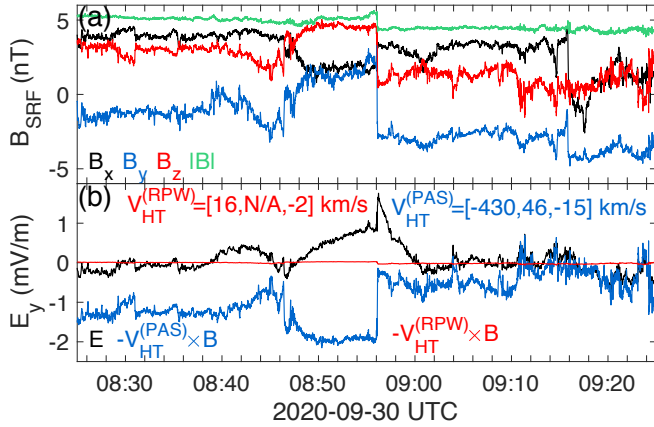


Fig. 4. Example of a failed HT analysis due to bad E_y data. Same format as Figs. 2a,b.

4. Solar wind velocity and the effective antenna length

As shown in Sect. 3, the shape of E_y is often well represented by $-(\mathbf{v}_{\text{HT}} \times \mathbf{B})_y$, while the magnitude $|E_y|$, and subsequently also v_{HT} , can be off by a scaling factor, which is likely related to the effective antenna length, L_{eff} . Understanding how L_{eff} varies with plasma conditions is therefore essential for our method to give as good velocity estimates as possible. In the following, we compare plasma velocities from PAS with the estimates from Eq. (2) to model L_{eff} .

Our procedure is as follows. When PAS, MAG, and RPW data are all available (discrete intervals between the end of May through October 2020), we take a ± 4 hour interval around a given time t_0 . In this interval we compute E_y according to the calibration method discussed in Sect. 2, and band-pass filter both E_y and \mathbf{B} between 0.139 mHz (2 hour period) and 0.3 Hz to get rid of potential problems associated with possible drifts of the probe offsets and any high-frequency noise. Applying Eq. (2) on the data within ± 30 min from t_0 , we finally obtain v_{HT} . We then take a step of ten minutes, $t_0 \rightarrow t_0 + 10$ [minutes], and repeat this process for all data to obtain a dataset of estimated solar wind velocities.

There are a few ways to quantify the quality of the obtained v_{HT} . The most straightforward ones are the correlation coefficient and the inclination of the linear slope between E_y and $-(\mathbf{v}_{\text{HT}} \times \mathbf{B})_y$. For the data to be considered of good quality, we require that the correlation coefficient is larger than 0.9, and that the inclination of the linear slope is between 0.95 and 1.05. In Fig. 4, we show an example of a failed HT analysis where clearly $E_y \neq -(\mathbf{v}_{\text{HT}} \times \mathbf{B})_y$. If the E_y data were good, the measured E_y (black) should have been in good agreement with $-(\mathbf{v}_{\text{HT}}^{(\text{RPW})} \times \mathbf{B})_y$ (red), and similar in shape (but potentially have a different magnitude due to L_{eff}) to $-(\mathbf{v}_{\text{HT}}^{(\text{PAS})} \times \mathbf{B})_y$ (blue). The cause of this behaviour has yet to be identified, but by using the above-mentioned quality measures we can discard intervals such as this one, for which the absolute value of the correlation coefficient is well below 0.9.

To estimate L_{eff} , we assume that v_x measured by PAS is exact, so that $v_{\text{HT},x}^{(\text{RPW})}/v_x = E_{y,\text{measured}}/E_{\text{real}} = L_{\text{eff}}/L_{23}$, where $E_{y,\text{measured}}$ is calculated using the nominal $L_{23} = 6.99$ m, and E_{real} is the physical electric field we would obtain by calculating E_y using L_{eff} . In Fig. 5a, using the data fulfilling our criteria for good quality, we plot L_{eff} against

$\lambda_{\text{De}} = \sqrt{\epsilon_0 T_e / (e^2 n_{\text{RPW}})}$, where e is the elementary charge, and we assume a constant electron temperature $T_e = 10$ eV, representative at 1 AU (Wilson et al. 2018), and n_{RPW} is the plasma density measured by RPW (Khotyaintsev et al. 2021). We see that L_{eff} can vary by several meters, which is in stark contrast to other missions such as Cluster, where L_{eff} was found to be close to constant (Khotyaintsev et al. 2014). This difference is likely due to the different probe and spacecraft geometries, and importantly, the relative length of the Debye length with respect to the probe-to-spacecraft separation. In particular, Solar Orbiter's E-field probes are cylindrical, close to the spacecraft, and in a plasma where the Debye length is comparable to the antenna length. In contrast, Cluster has spherical probes located around 40 meters away from the spacecraft and it samples the magnetosphere, where the Debye length is typically much larger than the probe-to-spacecraft separation. We also note that the effective antenna length of Parker Solar Probe, which has probes comparable to Solar Orbiter, has been found to be highly variable (Mozer et al. 2020a). While the observed range of L_{eff} is quite large, the results are reasonable in that $L_{\text{eff}} < 14$ m, which is the tip-to-tip distance of the probes as shown in Fig. 1. In addition, we see that for increasing Debye lengths L_{eff} tends to decrease and appears to converge to a steady value. Similarly, for Debye lengths approaching zero, we expect L_{eff} to reach a constant value, since the antennas will eventually be completely unaffected by the spacecraft potential, due to Debye shielding. However, there is not enough data at short λ_{De} to give a conclusive picture of the asymptotic behaviour. We note that the data from the beginning of June (dark-blue dots) are clustered at a significantly shorter L_{eff} compared to later data with similar Debye length. We believe this difference can be attributed to changes in the probe surface and photo-electron yield observed during the first perihelion.

We construct a simple semi-empirical model for L_{eff} of the form

$$L_{\text{eff}}(\lambda_{\text{De}}) = L_{\text{eff},\text{min}} + \frac{L_{\text{eff},\text{max}} - L_{\text{eff},\text{min}}}{1 + (\lambda_{\text{De}}/L_{\text{antenna}})^4}, \quad (4)$$

where $L_{\text{antenna}} = 6.5$ m is the length of each individual RPW antenna, and optimisation gives $L_{\text{eff},\text{min}} = 4.1$ m $L_{\text{eff},\text{max}} = 9.5$ m, which are the asymptotic values for long and short λ_{De} , respectively. This is of course just one of many possible equations to fit the data to, but we favor it due to its relative simplicity and the fact that $L_{\text{eff},\text{min}}$ and $L_{\text{eff},\text{max}}$ are within the limiting values expected by Fig. 1 (3.76 and 13.99 m respectively). We plot Eq. (4) in Fig. 5a in red. This model can serve as a first order approximation of L_{eff} . We use the model to correct the velocities in our dataset which satisfy the criteria for good quality described above, as $v_{\text{corrected}} = v_{\text{HT},x} L_{23} / L_{\text{eff}}$. We plot the relative error between $v_{\text{HT},x}$ and v_x before and after correction as histograms in Fig. 5b. The correction leads to a clear improvement, with the corrected data being centred around 0, and 71% of the corrected data has a relative error within $\pm 20\%$, and 90% of data within $\pm 30\%$. For the original data, these numbers are 58% and 81%, respectively.

5. Discussion

Our results open the door to the possibility of using magnetic and electric field data to estimate the solar wind speed in the absence of plasma measurements. For the method to give reliable results for a set of data, variations in the magnetic field due to current sheets or MHD turbulence as well as an estimate of the effective antenna length are crucial.

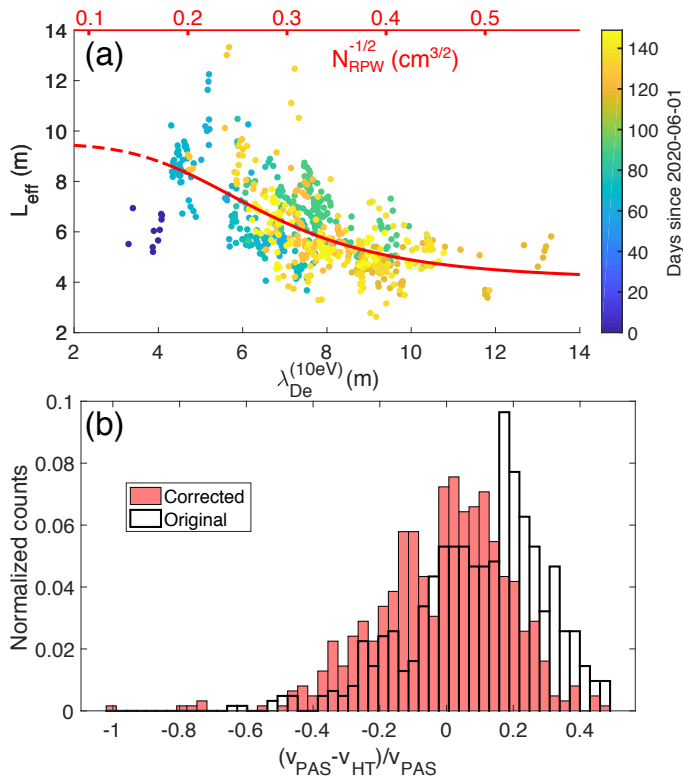


Fig. 5. Modelling the effective antenna length. *Panel a:* effective antenna length as a function of λ_{De} using densities from RPW from solar wind analysis. The time of each observation in units of days since 2020-06-01 are colour-coded. The solid red curve shows a fit to the data (see text for details), and the dashed curve shows the extrapolation. *Panel b:* relative error of solar wind speed before (white) and after (red) correcting for L_{eff} .

The need for magnetic fluctuations of substantial amplitude limits the time resolution of the computed solar wind velocity. In addition, by applying the HT method on sequential intervals, we often find v_{HT} to vary more than we expect the solar wind velocity to do. It is therefore often appropriate to average our velocities on the scale of a few hours. For these reasons we believe our method should primarily be used to estimate the solar wind speed and distinguish between fast and slow solar wind on a large scale. However, the method is very flexible, and could in principle be used to determine the phase speed of structures on a shorter time scale as well.

Our simple model of L_{eff} in Eq. (4) enables us to estimate L_{eff} using density measurements, which can be provided by the spacecraft potential and plasma frequency measured by RPW (Khotyaintsev et al. 2021). We note that the current model does not account for any variations in T_e or other effects depending on heliocentric distance. Kretzschmar et al. (2021) used **E** and **B** measurements of electromagnetic whistler waves to compute L_{eff} . Their results are in good agreement with our model. Their method could thus be important in the future to obtain local values of L_{eff} even if no plasma data are available.

6. Conclusions

In summary, we investigate the quality of the E_y -component of Solar Orbiter’s low frequency ‘DC’ electric field by applying a deHoffmann-Teller analysis to solar wind current sheets, one of which (likely to be the heliospheric current sheet) shows several signatures of ongoing magnetic reconnection. We conclude that

E_y is often accurate but can vary by a certain scaling factor which is likely related to the effective antenna length. By applying the deHoffmann-Teller analysis to estimate the solar wind velocity and comparing the results to measured plasma velocities, we are able to model how the effective antenna length depends on the Debye length. By applying this model, we can significantly improve our estimate of the solar wind speed, with 90% of measurements having relative errors below 30%.

Since we can use the RPW measurements of the spacecraft potential and plasma frequency to estimate the plasma density (Khotyaintsev et al. 2021), our results can be used in the future to measure the solar wind speed with sufficient accuracy to distinguish fast and slow solar wind, even in the absence of plasma measurements.

Acknowledgements. Solar Orbiter is a mission of international cooperation between ESA and NASA, operated by ESA. We thank the entire Solar Orbiter team and instrument PIs for data access and support. Solar Orbiter data are available at <http://soar.esac.esa.int/soar/#home>. This work is supported by the Swedish Research Council, grant 2016-05507, and the Swedish National Space Agency grant 20/136. G.C. is supported by Swedish National Space Agency contract SNSA 144/18, and Swedish Research Council contract VR 2018-03569. E.Y. is supported by the Swedish Civil Contingencies Agency, grant 2016-2102. The Solar Orbiter magnetometer was funded by the UK Space Agency (grant ST/T001062/1). T.H. is supported by STFC grant ST/S000364/1. The RPW instrument has been designed and funded by CNES, CNRS, the Paris Observatory, The Swedish National Space Agency, ESA-PRODEX and all the participating institutes. The Solar Orbiter Solar Wind Analyser (SWA) PAS were designed, created, and are operated under funding provided in numerous contracts from the UK Space Agency (UKSA), the UK Science and Technology Facilities Council (STFC), the Centre National d’Etudes Spatiales (CNES, France), the Centre National de la Recherche Scientifique (CNRS, France), and the Czech contribution to the ESA PRODEX programme. Data analysis was partly performed with the AMDA science analysis system provided by the Centre de Données de la Physique des Plasmas (CDPP) supported by CNRS, CNES, Observatoire de Paris and Université Paul Sabatier, Toulouse.

References

- Bale, S. D., Badman, S. T., Bonnell, J. W., et al. 2019, *Nature*, 576, 237
 Borovsky, J. E. 2010, *Phys. Rev. Lett.*, 105, 111102
 Cully, C. M., Ergun, R. E., & Eriksson, A. I. 2007, *J. Geophys. Res.: Space Phys.*, 112
 De Hoffmann, F., & Teller, E. 1950, *Phys. Rev.*, 80, 692
 Fox, N. J., & McComas, D. J. 2016, *Space Sci. Rev.*, 204, 1
 Froment, C., Krasnoselskikh, V., de Wit, T. D., et al. 2021, *A&A*, 650, A5
 Fuselier, S. A., Klumpp, D. M., & Shelley, E. G. 1991, *Geophys. Res. Lett.*, 18, 139
 Gosling, J. T., Skoug, R. M., McComas, D. J., & Smith, C. W. 2005, *J. Geophys. Res.: Space Phys.*, 110
 Horbury, T. S., Matteini, L., & Stansby, D. 2018, *MNRAS*, 478, 1980
 Horbury, T. S., Woolley, T., Laker, R., et al. 2020a, *ApJS*, 246, 45
 Horbury, T. S., O’Brien, H., Carrasco Blazquez, I., et al. 2020b, *A&A*, 642, A9
 Hudson, P. 1970, *Planet. Space Sci.*, 18, 1611
 Johansson, F. L., Eriksson, A. I., Gilet, N., et al. 2020, *A&A*, 642, A43
 Khotyaintsev, Y. V., Lindqvist, P.-A., Cully, C. M., Eriksson, A. I., & André, M. 2014, *Geosci. Instrum. Methods Data Syst.*, 3, 143
 Khotyaintsev, Yu. V., Graham, D. B., Vaivads, A., et al. 2021, *A&A*, 656, A19 (SO Cruise Phase SI)
 Khrabrov, A. V., & Sonnerup, B. U. 1998, *Analysis Methods for Multi-Spacecraft Data*, 1, 221
 Knetter, T., Neubauer, F. M., Horbury, T., & Balogh, A. 2004, *J. Geophys. Res.: Space Phys.*, 109
 Kretzschmar, M., Chust, T., Krasnoselskikh, V., Graham, D. B., et al. 2021, *A&A*, 656, A24 (SO Cruise Phase SI)
 Lavraud, B., Gosling, J. T., Rouillard, A. P., et al. 2009, *Sol. Phys.*, 256, 379
 Lefebvre, B., Schwartz, S. J., Fazakerley, A. F., & Décréau, P. 2007, *J. Geophys. Res.: Space Phys.*, 112
 Maksimovic, M., Bale, S. D., Chust, T., et al. 2020, *A&A*, 642, A12
 Mozer, F. S., Agapitov, O. V., Bale, S. D., et al. 2020a, *J. Geophys. Res.: Space Phys.*, 125, e2020JA027980
 Mozer, F. S., Agapitov, O. V., Bale, S. D., et al. 2020b, *ApJS*, 246, 68

- Müller, D., St. Cyr, O. C., Zouganelis, I., et al. 2020, *A&A*, **642**, A1
- Němeček, Z., Ďurovcová, T., Šafránková, J., et al. 2020a, *ApJ*, **889**, 163
- Němeček, Z., Ďurovcová, T., Šafránková, J., et al. 2020b, *ApJ*, **897**, L39
- Owen, C. J., Bruno, R., Livi, S., et al. 2020, *A&A*, **642**, A16
- Paschmann, G., & Sonnerup, B. U. 2008, *ISSI Sci. Rep. Ser.*, **8**, 65
- Phan, T. D., Dunlop, M. W., Paschmann, G., et al. 2004, *Ann. Geophys.*, **22**, 2355
- Phan, T. D., Bale, S. D., Eastwood, J. P., et al. 2020, *ApJS*, **246**, 34
- Rouillard, A. P., Pinto, R. F., Vourlidas, A., et al. 2020, *A&A*, **642**, A2
- Schwartz, S. J., Thomsen, M. F., Bame, S. J., & Stansberry, J. 1988, *J. Geophys. Res.: Space Phys.*, **93**, 12923
- Sonnerup, B. U., & Cahill, L. J. Jr. 1967, *J. Geophys. Res. (1896-1977)*, **72**, 171
- Sonnerup, B. U. Ö., Papamastorakis, I., Paschmann, G., & Lühr, H. 1987, *J. Geophys. Res.: Space Phys.*, **92**, 12137
- Wilson, L. B., III, Stevens, M. L., Kasper, J. C., et al. 2018, *ApJS*, **236**, 41
- ⁵ Space Sciences Laboratory, University of California, Berkeley, CA, USA
- ⁶ Physics Department, University of California, Berkeley, CA, USA
- ⁷ LPP, CNRS, Ecole Polytechnique, Sorbonne Université, Observatoire de Paris, Université Paris-Saclay, Palaiseau, Paris, France
- ⁸ LPC2E, CNRS, 3A avenue de la Recherche Scientifique, Orléans, France
- ⁹ Université d'Orléans, Orléans, France
- ¹⁰ CNES, 18 avenue Edouard Belin, 31400 Toulouse, France
- ¹¹ Technische Universität Dresden, Helmholtz Str. 10, 01187 Dresden, Germany
- ¹² Institute of Atmospheric Physics of the Czech Academy of Sciences, Prague, Czech Republic
- ¹³ Space Research Institute, Austrian Academy of Sciences, Graz, Austria
- ¹⁴ Astronomical Institute of the Czech Academy of Sciences, Prague, Czech Republic
- ¹⁵ Radboud Radio Lab, Department of Astrophysics, Radboud University, Nijmegen, The Netherlands
- ¹⁶ Imperial College London, South Kensington Campus, London SW7 2AZ, UK
- ¹⁷ Institut de Recherche en Astrophysique et Planétologie, 9 avenue du Colonel Roche, BP 4346, 31028 Toulouse Cedex 4, France
- ¹⁸ Laboratoire d'astrophysique de Bordeaux, Univ. Bordeaux, CNRS, Pessac, France
- ¹⁹ Mullard Space Science Laboratory, University College London, Holmbury St. Mary, Dorking, Surrey RH5 6NT, UK
-
- ¹ Swedish Institute of Space Physics (IRF), Uppsala 75121, Sweden
e-mail: konrad.steinvall@irfu.se
- ² Space and Plasma Physics, Department of Physics and Astronomy, Uppsala University, Uppsala 75120, Sweden
- ³ Division of Space and Plasma Physics, School of Electrical Engineering and Computer Science, KTH Royal Institute of Technology, Stockholm 11428, Sweden
- ⁴ LESIA, Observatoire de Paris, Université PSL, CNRS, Sorbonne Université, Univ. Paris Diderot, Sorbonne Paris Cité, 5 place Jules Janssen, 92195 Meudon, France